Lithuanian Journal of Physics, Vol. **48**, No. 2, pp. 163–176 (2008)

SPIN PROPERTIES OF FREE ELECTRONS AND HOLES IN $Hg_{1-x}Cd_xTe$ / CdTe QUANTUM WELL

A. Dargys

Semiconductor Physics Institute, A. Goštauto 11, LT-01108 Vilnius, Lithuania
E-mail: dargys@pfi.lt

Received 17 February 2008; accepted 9 June 2008

Spin properties of $Hg_{1-x}Cd_xTe$ / CdTe quantum wells (QW) with inverted energy bands are considered using eight-band $\mathbf{k}\cdot\mathbf{p}$ Hamiltonian. The spin splitting of doubly degenerate bands (Kramers pairs) was included via either Rashba or external voltage Hamiltonians. The spin surfaces, which describe the average spin as a function of spin direction of a ballistic 2D charge carrier, in general, are shown to be ellipsoidal rather than spherical. In extreme cases the spin surfaces may reduce to disk, line, or Bloch sphere. Characteristic shapes of the spin surfaces at different wave vectors and QW composition x are presented in a form of graphs in the spin space.

Keywords: spintronics, spin–orbit coupling, spin models, II–VI semiconductors, spin-FET

PACS: 85.75.-d, 85.75.Hh, 75.10.Hk, 73.61.Ga

1. Introduction

Passive spin components (filters, spin guides, bends, couplers, etc.) and active devices (spin-FETs) are required in solid-state spintronics to transmit and control electron and hole spin polarization [1–3]. Spin–orbit (SO) interaction that couples charge current and spin polarization is the main mechanism to control electron and hole spins by external electric fields in these devices. In the paper [4] a critical analysis of the main pitfalls encountered in realizing the spin-FET were revealed. Specifically, it was pointed out that the spin surface, which is an analogue of the Bloch sphere [5], is a very useful object to describe global properties of the charge carrier spin. The knowledge of the spin surface allows one to envisage possible trajectories in spin devices as well as to make some judgements about the matching conditions of spins at an interface between different materials. Up till now, attempts to realize the spin-FET in a form proposed by Datta and Das [6] were unsuccessful. Very recently, however, it was experimentally demonstrated that spin precession of hot electrons in silicon can modulate the channel conductivity [7, 8]. Apart from elementary semiconductors and A_3B_5 compounds the spin properties of which are extensively studied [1–3], there is a group of narrow or zero gap semiconductors that may be of interest to spintronics, namely, the inverted band semiconductors represented by HgTe. Very recently HgTe / $Hg_{0.3}Cd_{0.7}Te$ QWs were used to prove experimentally a new, the so-called quantum spin Hall effect [9, 10], where the helical edge state transport might be possible even in the absence of the external magnetic fields.

In this paper we shall be interested in $Hg_{1-x}Cd_xTe$ / CdTe QWs the lattice of which possesses zinc-blende symmetry. In HgTe the conduction band of Γ_6 symmetry is separated from the valence band by the negative energy gap E_g and at the same time is inverted upside-down as shown in Fig. 1(a). The light-mass band of symmetry Γ_8 is inverted too and plays the role of the conduction band. The inverted energy bands in $Hg_{1-x}Cd_xTe$ appear when $x < 0.18$. At these values of x the QW consists of CdTe barriers with positive (normal) band gap and of $Hg_{1-x}Cd_xTe$ well with inverted bands as shown in Fig. 1(b). Spatial quantization of the wave function in the well gives rise to 2D electron and hole energy subbands, where interplay between the inverted and normal bands arises. If $Hg_{1-x}Cd_xTe$ bands are inverted, two distinct heterostructure regimes can be realized [12–17]. When $Hg_{1-x}Cd_xTe$ quantum well is thin enough then the first electronic subband E1 is pushed up high enough, above the first heavy-hole energy subband H1. The QW in this case, despite band inversion in the well material, in fact appears as a normal semiconductor. However, in thick HgTe wells the first heavy-hole subband H1 rises

ISSN 1648-8504

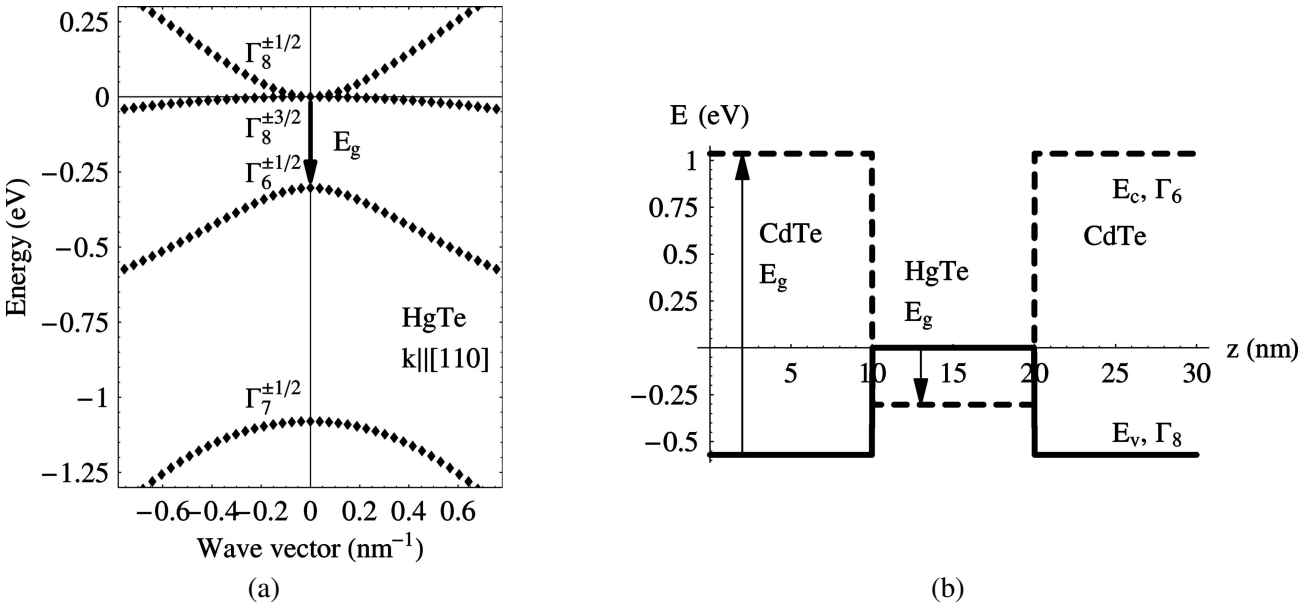

Fig. 1. (a) The inverted band structure of bulk HgTe, where band symmetry nomenclature is indicated. (b) Conduction (dashed line) and valence (solid line) band edge profiles in CdTe / HgTe / CdTe quantum well. In CdTe the gap E_g is positive, while in HgTe it is negative, as shown by up and down arrows, respectively. The inverted 2D subbands in the QW appear when the width of the QW is approximately larger than 7.2 nm.

above E1. In this case one has the inverted 2D subband regime even at large kinetic energies of the electrons. Concrete values of the critical well thickness can be found from band edge intersection. In Fig. 2, the dependence of the subband edge energies on QW width is plotted in the case of HgTe / CdTe QW, where it is seen that at well width 7.2 nm the conduction E1 and valence H1 subbands intersect and at larger well widths the role of the lowest conduction band is played by the hole H1 subband. For $Hg_{0.3}Cd_{0.7}Te$ / HgTe QW the critical thickness is 6.3 nm [10]. Below we shall be interested in inverted 2D semiconductors represented by $Hg_{1-x}Cd_xTe$ / CdTe, where the giant Rashba SO splitting in electronic 2D structures have recently aroused much interest due to their possible application in spintronics [11–17]. The Rashba spin-splitting of up to 30 meV has been measured, which is almost an order of magnitude larger than in A_3B_5 compounds [2].

In Refs. [4, 18] it has been shown that SO interaction brings about strong nonsphericity in the spin surfaces, especially in the valence bands where band rearrangement in the center of the Brillouin zone frequently takes place. Since in $Hg_{1-x}Cd_xTe$ / CdTe QWs the light-mass band plays the role of the conduction band, one expects that spin surfaces of the conduction band will be deformed strongly too. In case of normal band ordering, for example in A_3B_5 compounds, the conduction band spin surfaces are close to spherical and in this case the Bloch sphere can be used to represent free electron spin precession and spin dynamics under external excitation as shown in Ref. [19]. As we shall see below, in the inverted band semiconductors the situation is different.

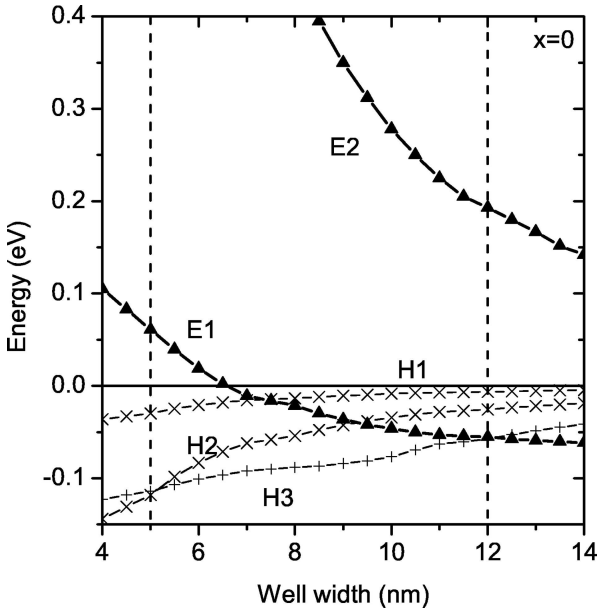

Fig. 2. Dependence of 2D conduction E1–E2 and valence H1–H3 subband edge energies on the well width in CdTe / HgTe QWs. Note that at well width 7.2 nm the E1 subband intersects with H1 valence subband. The spectra at dotted vertical lines are shown in Fig. 3.

In the next section using $\mathbf{k} \cdot \mathbf{p}$ and Rashba Hamiltonians the spectrum of 2D electrons and holes is investigated in $Hg_{1-x}Cd_xTe$ / CdTe QWs at well width of 12 nm. In Secs. 3 and 4 the needed spin–orbital

matrices and parametrized spinors are constructed. Finally, in Sec. 5 the results of numerical calculations in a form of spin surfaces in the spin space are presented and examined. In this article only the case when the QW subbands are in the inverted regime will be considered. The preliminary results were published in the letter [20].

2. Basis functions and Hamiltonians

The band structure needed for numerical calculations below is based on an envelope function approach introduced by Burt [21] and applied by Foreman [22] to take boundary conditions in zinc-blende-type semiconductors correctly. The corresponding basis functions in the centre of the Brillouin zone in the total angular momentum **J** representation $|J, m_J\rangle$, where m_J is the azimuthal quantum number, are (see Fig. 1(b) for band symmetry nomenclature):

$$
\begin{aligned}
|\Gamma_6, +1/2\rangle &= (1/\sqrt{3})|S\uparrow\rangle\,,\\
|\Gamma_6, -1/2\rangle &= (1/\sqrt{3})|S\downarrow\rangle\,,\\
|\Gamma_8, +3/2\rangle &= (1/\sqrt{2})|(X+\mathrm{i}Y)\uparrow\rangle\,,\\
|\Gamma_8, +1/2\rangle &= (1/\sqrt{6})\left(|(X+\mathrm{i}Y)\downarrow\rangle - 2|Z\uparrow\rangle\right)\,,\\
|\Gamma_8, -1/2\rangle &= -(1/\sqrt{6})|(X-\mathrm{i}Y)\uparrow\rangle + 2|Z\downarrow\rangle\,,\\
|\Gamma_8, -3/2\rangle &= -(1/\sqrt{2})|(X-\mathrm{i}Y)\downarrow\rangle\,,\\
|\Gamma_7, +1/2\rangle &= (1/\sqrt{3})\left(|(X+\mathrm{i}Y)\downarrow\rangle + |Z\uparrow\rangle\right)\,,\\
|\Gamma_7, -1/2\rangle &= (1/\sqrt{3})\left(|(X-\mathrm{i}Y)\uparrow\rangle - |Z\downarrow\rangle\right)\,,
\end{aligned}
\tag{1}
$$

where Γ_i, m_J in the kets indicate, respectively, the representation and projection of the angular momentum. The orbitals $|X\rangle$, $|Y\rangle$, and $|Z\rangle$ transform as Cartesian coordinates x, y, and z, and $|S\rangle$ is totally symmetric. The exact expressions for these functions are not required in the following. The up and down arrows indicate two spin states. The basis (1) is orthonormalized.

The Hamiltonian with [001] growth direction takes the following form in the above basis [22, 23]:

$$
H_0 = \left[\begin{array}{cc|cccc|cc}
T & 0 & -\frac{1}{\sqrt{2}}Pk_+ & \sqrt{\frac{2}{3}}Pk_z & \frac{1}{\sqrt{6}}Pk_- & 0 & -\frac{1}{\sqrt{3}}Pk_z & -\frac{1}{\sqrt{3}}Pk_- \\
0 & T & 0 & -\frac{1}{\sqrt{6}}Pk_+ & \sqrt{\frac{2}{3}}Pk_z & \frac{1}{\sqrt{2}}Pk_- & -\frac{1}{\sqrt{3}}Pk_+ & \frac{1}{\sqrt{3}}Pk_z \\
\hline
-\frac{1}{\sqrt{2}}k_-P & 0 & U+V & -\overline{S}_- & R & 0 & \frac{1}{\sqrt{2}}\overline{S}_- & -\sqrt{2}R \\
\sqrt{\frac{2}{3}}k_zP & -\frac{1}{\sqrt{6}}k_-P & -\overline{S}_-^\dagger & U-V & C & R & \sqrt{2}V & -\sqrt{\frac{3}{2}}\tilde{S}_- \\
\frac{1}{\sqrt{6}}k_+P & \sqrt{\frac{2}{3}}k_zP & R^\dagger & C^\dagger & U-V & \overline{S}_+^\dagger & -\sqrt{\frac{3}{2}}\tilde{S}_+ & -\sqrt{2}V \\
0 & \frac{1}{\sqrt{2}}k_+P & 0 & R^\dagger & \overline{S}_+ & U+V & \sqrt{2}R^\dagger & \frac{1}{\sqrt{2}}\overline{S}_+ \\
\hline
-\frac{1}{\sqrt{3}}k_zP & -\frac{1}{\sqrt{3}}k_-P & \frac{1}{\sqrt{2}}\overline{S}_-^\dagger & \sqrt{2}V & -\sqrt{\frac{3}{2}}\tilde{S}_+^\dagger & \sqrt{2}R & U-\Delta & C \\
-\frac{1}{\sqrt{3}}k_+P & \frac{1}{\sqrt{3}}k_zP & -\sqrt{2}R^\dagger & -\sqrt{\frac{3}{2}}\tilde{S}_-^\dagger & -\sqrt{2}V & \frac{1}{\sqrt{2}}\overline{S}_+^\dagger & C^\dagger & U-\Delta
\end{array}\right]\,,
\tag{2}
$$

where three diagonal blocks correspond to, respectively, conduction, valence, and SO split-off bands. The coordinate z is assumed to be perpendicular to the QW plane. The in-plane wave vector is characterized by $k_\pm = k_x \pm \mathrm{i}k_y$ and $k_\parallel^2 = k_x^2 + k_y^2$, while the perpendicular to QW wave vector is represented by the differential operator $k_z = -\mathrm{i}\partial/\partial z$. The other symbols in Eq. (2) are:

$$T = E_{\rm c} + \frac{\hbar^2}{2m_0}\left[(2F+1)k_\parallel^2 + k_z(2F+1)k_z\right], \quad (3)$$

$$U = E_{\rm v} - \frac{\hbar^2}{2m_0}\left(\gamma_1 k_\parallel^2 + k_z\gamma_1 k_z\right), \quad (4)$$

$$V = -\frac{\hbar^2}{2m_0}\left(\gamma_2 k_\parallel^2 - 2k_z\gamma_2 k_z\right), \quad (5)$$

$$R = -\frac{\hbar^2}{2m_0}\sqrt{3}\left(\mu k_+^2 - \overline{\gamma}k_-^2\right), \quad (6)$$

$$\overline{S}_\pm = -\frac{\hbar^2}{2m_0}\sqrt{3}k_\pm\left(\{\gamma_3, k_z\} + [\kappa, k_z]\right), \quad (7)$$

$$\tilde{S}_\pm = -\frac{\hbar^2}{2m_0}\sqrt{3}k_\pm\left(\{\gamma_3, k_z\} - \frac{1}{3}[\kappa, k_z]\right), \quad (8)$$

$$C = \frac{\hbar^2}{m_0}\, k_-\,[\kappa, k_z], \quad (9)$$

$$\mu = \frac{\gamma_3 - \gamma_2}{2}, \quad (10)$$

$$\overline{\gamma} = \frac{\gamma_3 + \gamma_2}{2}. \quad (11)$$

Here $[A, B] = AB - BA$ is the commutator and $\{A, B\} = AB + BA$ is the anticommutator. P is the Kane momentum matrix element. The conduction $E_{\rm c}$ and valence $E_{\rm v}$ band edges, Fig. 1(b), spin–orbit splitting energy Δ, and the valence–conduction band parameters γ_1, γ_2, γ_3, κ, and F are functions of the coordinate z. It is assumed that the band structure parameters change abruptly at the interface. The parameter F is related to the conduction-band-edge mass via $m_{\rm c}/m_0 = 1/(2F+1)$. The parameter κ is expressed through valence band parameters, $\kappa = (-1 - \gamma_1 + 2\gamma_2 + 3\gamma_3)/3$. In the bulk materials, the commutator $[\kappa, k_z]$ is equal to zero and in this case one has $C = 0$, $\overline{S}_\pm = \tilde{S}_\pm = -(\hbar^2/m_0)\sqrt{3}\gamma_3 k_\pm k_z$. The parameter $\mu = (\gamma_3 - \gamma_2)/2$ describes the magnitude of valence band warping. The Hamiltonian (2) gives doubly spin-degenerate bands, i. e. Kramers doublets. At $\mathbf{k} = 0$ the valence band has symmetry Γ_8. In HgTe, at $\mathbf{k} \neq 0$ the valence band splits into heavy-mass and inverted light-mass bands, i. e. electron-like bands in the following denoted as $\Gamma_8^{\pm 3/2}$ and $\Gamma_8^{\pm 1/2}$, respectively. The band $\Gamma_6^{\pm 1/2}$, which in A_3B_5 compounds plays the role of the conduction band, in HgTe is also inverted and shifted down in energy by 0.303 eV. The spin split-off valence band is below by 1.08 eV from Γ_8 point.

Table 1. Band structure parameters of $Hg_{1-x}Cd_xTe$ / CdTe quantum wells. $E_{\rm g}$ is the energy gap, Δ is the spin–orbit splitting energy, Λ is the valence band offset, $E_p = 2m_0P^2/\hbar^2$ is the energy related to the Kane momentum matrix element P, F is related to the conduction band effective mass, γ_i's are valence band parameters, r_i's are the Rashba coefficients.

	HgTe	$Hg_{0.3}Cd_{0.7}Te$	CdTe
$E_{\rm g}$ (eV)	-0.303	1.006	1.606
Δ (eV)	1.08	0.961	0.91
Λ (eV)	0	0.404	0.577
E_p (eV)	18.8	18.8	18.8
$m_{\rm c}$	0.02	0.045	0.096
F	24.5	10.6	4.7
γ_1	4.1	2.26	1.47
γ_2	0.5	-0.046	-0.28
γ_3	1.3	0.411	0.03
$r_{\rm c}$ (eV nm)		0.1	
$r_{\rm v}$ (eV nm)		0.1	
$r_{\rm s}$ (eV nm)		0.1	
$r_{\rm vs}$ (eV nm)		0.1	

The band structure parameters are listed in Table 1. In mercury-rich $Hg_{1-x}Cd_xTe$ alloys the parameters were obtained by linear interpolation, except for the energy bandgap. In $Hg_{1-x}Cd_xTe$ the dependence of the gap $E_{\rm g}$ on temperature T and composition x was approximated by empirical formula [24]

$$E_{\rm g}({\rm eV}) = -0.303(1-x) + 1.606x - 0.132x(1-x) + \frac{[6.3(1-x) - 3.25x - 5.92x(1-x)]\cdot 10^{-4}T^2}{11(1-x) + 78.7x + T}. \quad (12)$$

As mentioned, the energy will be referenced with respect to valence band edge in the QW, Fig. 1(b). From this figure one reads

$$E_{\rm c}(z) = \begin{cases} E_{\rm g}({\rm CdTe}) - \Lambda > 0 & \text{in the barrier}, \\ E_{\rm g}({\rm HgTe}) > 0 & \text{in the well}, \end{cases} \quad (13)$$

$$E_{\rm v}(z) = \begin{cases} -\Lambda < 0 & \text{in the barrier}, \\ 0 & \text{in the well}, \end{cases} \quad (14)$$

where Λ is the valence band offset at the barrier–well interface.

The spin-splitting of the 2D bands may arise from the absence of inversion symmetry in the constituent layers (bulk asymmetry) and the QW asymmetry (structural asymmetry). The latter may be induced by the stress field, internal or external electric field in the direction perpendicular to the QW, or may be inherent to the QW itself (Rashba spin-splitting), for example, due to different arrangement of atoms in opposite interfaces. Large electric field-induced spin-splitting effect in narrow-gap HgCdTe was observed

for the first time in the oscillatory magnetoconductivity experiments by Wollrab et al. [25]. Later, in papers [13, 15, 17, 23, 26, 27] this was confirmed in various experiments with HgTe / CdTe QW's, where the spin-splitting energy as high as 30 meV was observed. Here we shall mainly be concerned with the Rashba spin-splitting and electric field induced spin-splitting in the QWs.

The Rashba Hamiltonian for 8-band zinc-blende semiconductor was considered by the invariant method in the book [28]. If has been found that the most general form of the Rashba Hamiltonian for the zinc-blende lattice may have as many as ten free parameters. Estimation of the magnitudes of these parameters for various semiconductors shows that only five–six of them are important. Below, in writing the Rashba Hamiltonian only the leading ones were included (r_{41}^{6c6c}, r_{41}^{8v8v}, r_{41}^{7v7v}, and r_{51}^{8v7v} in the notation of the book [28]). Here the reduced Hamiltonian, when the Rashba field is parallel to z axis, will be used. Then, in the basis $|Jm_J\rangle = \left(|\frac{1}{2}\frac{1}{2}\rangle, |\frac{1}{2}\frac{\overline{1}}{2}\rangle, |\frac{3}{2}\frac{3}{2}\rangle, |\frac{3}{2}\frac{1}{2}\rangle, |\frac{3}{2}\frac{\overline{1}}{2}\rangle, |\frac{3}{2}\frac{\overline{3}}{2}\rangle, |\frac{1}{2}\frac{1}{2}\rangle, |\frac{1}{2}\frac{\overline{1}}{2}\rangle\right)$ the Rashba Hamiltonian assumes the form

$$H_{\rm R} = \left[\begin{array}{cc|cccc|cc} 0 & \mathrm{i}r_{\rm c}k_- & 0 & 0 & 0 & 0 & 0 & 0 \\ -\mathrm{i}r_{\rm c}k_+ & 0 & 0 & 0 & 0 & 0 & 0 & 0 \\ \hline 0 & 0 & 0 & -\mathrm{i}\frac{\sqrt{3}}{2}r_{\rm v}k_- & 0 & 0 & -\frac{\mathrm{i}}{\sqrt{6}}r_{\rm vs}k_- & 0 \\ 0 & 0 & \mathrm{i}\frac{\sqrt{3}}{2}r_{\rm v}k_+ & 0 & -\mathrm{i}r_{\rm v}k_- & 0 & 0 & -\frac{\mathrm{i}}{3\sqrt{2}}r_{\rm vs}k_- \\ 0 & 0 & 0 & \mathrm{i}r_{\rm v}k_+ & 0 & -\mathrm{i}\frac{\sqrt{3}}{2}r_{\rm v}k_- & -\frac{\mathrm{i}}{3\sqrt{2}}r_{\rm vs}k_+ & 0 \\ 0 & 0 & 0 & 0 & \mathrm{i}\frac{\sqrt{3}}{2}r_{\rm v}k_+ & 0 & 0 & -\frac{\mathrm{i}}{\sqrt{6}}r_{\rm vs}k_+ \\ \hline 0 & 0 & \frac{\mathrm{i}}{\sqrt{6}}r_{\rm vs}k_+ & 0 & \frac{\mathrm{i}}{3\sqrt{2}}r_{\rm vs}k_- & 0 & 0 & \mathrm{i}r_{\rm s}k_- \\ 0 & 0 & 0 & \frac{\mathrm{i}}{3\sqrt{2}}r_{\rm vs}k_+ & 0 & \frac{\mathrm{i}}{\sqrt{6}}r_{\rm vs}k_- & -\mathrm{i}r_{\rm s}k_+ & 0 \end{array}\right], \qquad (15)$$

where $r_{\rm c}$, $r_{\rm v}$, and $r_{\rm s}$ are the Rashba coefficients for conduction, valence, and spin–orbit split-off bands and $r_{\rm vs}$ includes the coupling between the bands. In the Hamiltonian (15) the leading terms are linear in the wave vector $k_\pm = k_x \pm \mathrm{i}k_y$.

The calculations were also repeated when the spin-splitting is induced by externally applied voltage $V_{\rm b}$ over the structure. The respective potential was assumed to change linearly with the coordinate z in the diagonal Hamiltonian,

$$H_{\rm R} = e\,V_{\rm b}\,(z/L)\,I, \qquad (16)$$

where L is the total transverse length of the structure and I is (8×8) unit matrix. The full Hamiltonian of the problem is equal to the sum of both Hamiltonians,

$$H = H_0 + H_{\rm R}\,. \qquad (17)$$

The mercury chalcogenide lattice does not possess the inversion symmetry. This asymmetry brings an additional contribution to the spin-splitting that is included through cubic in the wave vector terms in the Hamiltonian (the Dresselhaus contribution [29]). The available experimental data indicate that the spin-splitting in bulk mercury telluride should be very small [26]. Thus, spin precession due to Dresselhaus contribution, if any, should be negligible too. On the other hand, the spin-splitting in asymmetric *n*-type HgTe single quantum wells, due to Rashba mechanism in combination with the inverted band structure, was found to be very large [12, 25–27]. By this reason we shall neglect the Dresselhaus contribution altogether.

2.1. Boundary conditions and method of solution

The wave functions (envelope functions) of the Hamiltonian (17) should remain continuous in the transition from the well to barrier layers. Also the derivatives with respect to coordinate z should be continuous. As shown by Burt [21] and Foreman [22] the correct rather than *ad hoc* symmetrization of the operators in the Hamiltonian provides an unambiguous determination of the boundary conditions at the interface. The required derivative matrix was presented in [23]. It should be noted that the required boundary conditions are automatically satisfied through the (correct) operator ordering in the Hamiltonian (2), since the Hamiltonian (2) contains apart from the symmetrized terms the additional off-diagonal elements $[\kappa(z), k_z]$, which are equal to zero in the bulk structures. Therefore, in the numerical calculations the approximation of derivatives by finite differences and subsequent expansion of the Hamiltonian on a large mesh automatically takes

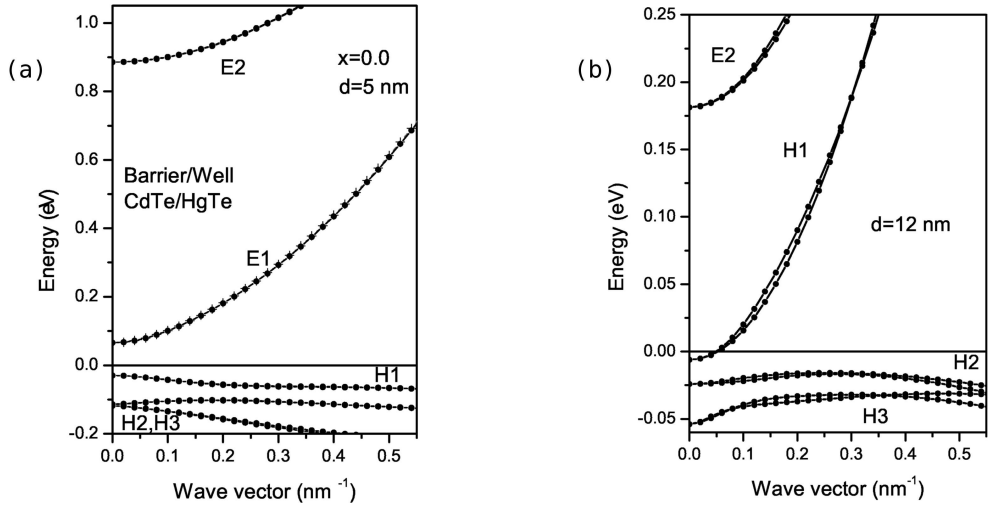

Fig. 3. Dispersion of main electron and hole subbands in QWs at two well widths: (a) $d = 5$ nm and (b) $d = 12$ nm. Zero of the energy is referenced to valence band edge in the well (see Fig. 1(b)).

into account the correct boundary conditions. For further discussion on this point see the Ref. [30].

The finite difference method was used to discretize the wave function and its derivatives. After the discretization the resulting Hamiltonian had a blocked structure. The Hamiltonian consisted of (8×8) diagonal blocks that corresponded to mesh points z_n, and adjacent upper and lower (8×8) blocks that corresponded to mesh points z_{n+1} and z_{n-1}, respectively. The potential of the first and the last points on the mesh has been assumed infinite, what is equivalent to nullifying the wave functions at the extreme ends of the barriers. At a given wave vector the spectrum of such Hamiltonian is discrete. Only those energy levels and wave functions that lie in the quantum well are physically meaningful and are consistent with the infinite lengths of the barriers, where all wave functions of the QW energy levels should decay exponentially. Discretized and expanded in this way Hamiltonian gives the correct eigenvalues if the discretization step is small enough and the magnitudes of wave functions in the extreme ends of the barriers are negligible.

Singular value decomposition (SVD) has been used to find the eigenvalues and corresponding eigenfunctions of the total Hamiltonian (17). For solutions to be meaningful, the SVD algorithm requires all eigenvalues to be positive [31]. Therefore, a constant energy was added to diagonal elements of the Hamiltonian (17) to shift all spectrum to positive values. This has no influence on the eigenfunctions and spin properties.

2.2. Spectrum and probability distribution

Figures 3 and 4 show the energy of main 2D electron and hole subbands as a function of the wave vector parallel to [10] in-plane crystallographic direction. In Fig. 3 the spectra were calculated for two different widths of the QW. At short well width, $d = 5$ nm, the energies of electronic (E1, E2) and hole (H1, H2, and H3) subbands are positive and negative, and are separated by energy gap, i. e. their character bears resemblance to the standard 2D spectral structure. At $d = 12$ nm, Fig. 3(b), the bands are inverted. As a result the subband edge energy of the electron E1 subband becomes negative (see Fig. 3). The dispersion of E1 band becomes flat and therefore disappears at the energy scale of the Fig. 3(b). On the other hand, the H1 subband becomes electron-like. However, as we shall see from spin properties of this subband, the valence band character of its wave function is preserved at small wave vectors only. At large wave vectors the wave function gradually acquires the conduction band character. In other words the H1 band is a mixture of conduction and valence bands, with heavy-hole valence band character prevailing only at low electron energies. In Fig. 3(b) the barrier material is $Hg_{0.3}Cd_{0.7}Te$. The properties of the wells with CdTe barriers were found to be similar.

When the Rashba Hamiltonian (15) is included, the double degeneracy of the subbands is lifted (spin-splitting). The splitting is better seen in Fig. 3(b). In H1 and H2 subbands the splitting goes through maximum while in E2 subband it monotonously increases with the wave vector. According to experiments [14] the Rashba coefficient is $r = (0.05 - 0.2)$ eV nm. The

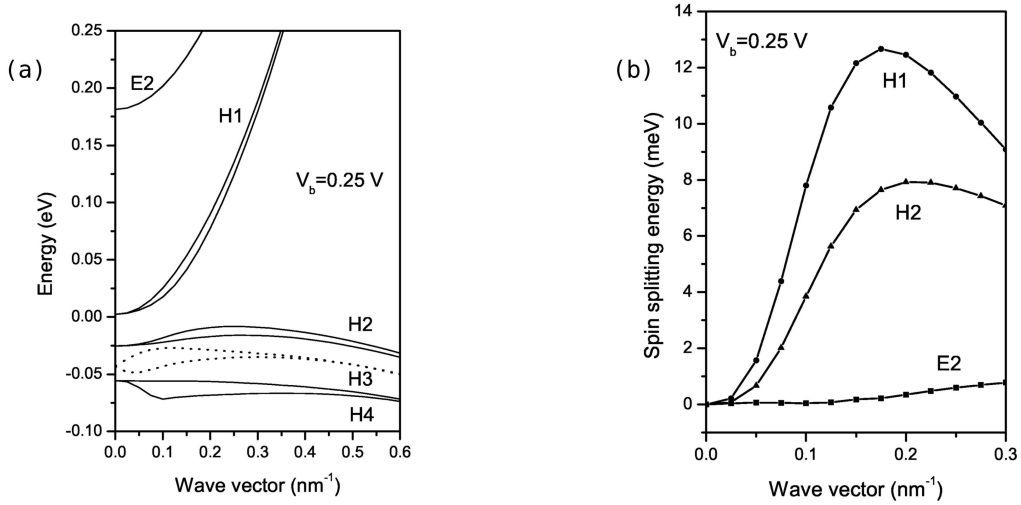

Fig. 4. (a) Dispersion of the lowest conduction, E2 and H1, and valence, H2, H3, and H4, bands and (b) spin-splitting in HgTe/$Hg_{0.3}Cd_{0.7}Te$ QW when the bias voltage (see the Hamiltonian (16)) of the amplitude 0.25 V was applied over the structure. $\mathbf{k}\|[10]$, $d = 12$ nm.

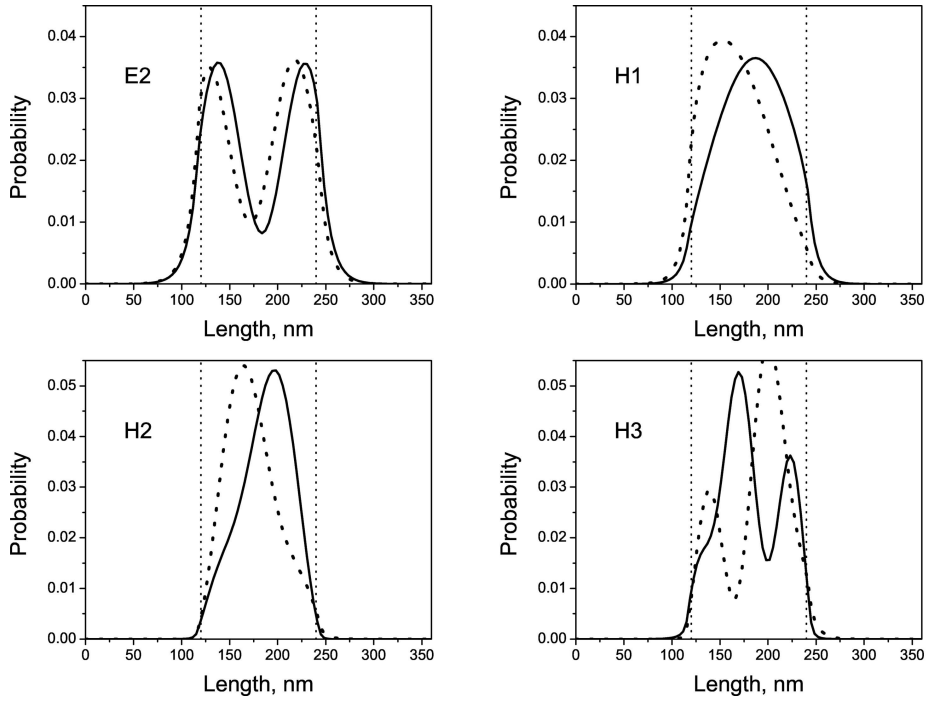

Fig. 5. Probability distribution density in the subbands E2, H1, H2, and H3 at the wave vector $\mathbf{k}\|[11]$ and $|\mathbf{k}|$=0.15 nm^{-1}. The vertical lines show well–barrier interface.

values $r_{\mathrm{c}} = r_{\mathrm{v}} = r_{\mathrm{s}} = r_{\mathrm{vs}} \equiv r = 0.1$ eV nm were used. In Ref. [20] the expanded view of the dependence of spin-splitting energy on wave vector was given.

The external electric field also brings about spin-splitting. The effect of an external bias V_{b} (Hamiltonian (16)) on the subband spectrum is shown in Fig. 4 for QW of width $d = 12$ nm. As in the Fig. 3, the energy of the first heavy-hole subband H1 is inverted (electron-like) and lies above the first electronic subband E1 (not shown in the figure). In Fig. 4(b) the spin-splitting in the structure is caused by electric field $\approx 70\ \mathrm{kV/cm}$ (the Rashba interaction $r = 0$ was set in this case). No space charge effects were included and the external electric field was assumed to be constant over the structure.

Figure 5 shows the probability density distribution in two main conduction (E2, H1) and two valence (H2, H3) subbands of the QW, when the spin-splitting is included through the Rashba matrix (15). In these and in subsequent figures the QW width was assumed to

be $d = 12$ nm and the length of total structure $L = 36$ nm. The pairs of the probability distributions (solid and dotted lines) in Fig. 5 correspond to spin-split energy subbands (see Fig. 4). As it should be, it has been found that the number of maxima and minima grows with the subband number, however, the distribution does not reach zero as is the case with simple quantum systems. The Hamiltonian $H_{\rm R}$ has negligible effect on general probability distributions shown in the Fig. 5 for SO coupling values used in this article.

3. Spin and orbital matrices

In the absence of SO interaction the energy bands are doubly degenerate. As follows from the Kramers theorem [32], the origin of which comes from time-reversal symmetry, the doubly degenerate band eigenspinors correspond to two spin states with the average spins pointing in the opposite directions. The concrete spin direction in the real space, however, does not necessarily coincide with the z axis, since now the spin depends on carrier wave vector $\mathbf{k}$ and the selected energy subband. Within Kramers degenerate subbands, the superpositions of the eigenstates do not change the eigenenergy $E(\mathbf{k})$. However, the direction of the average spin as well as its magnitude, in general, will depend on a selected superposition. In the absence of SO interaction, the two-component spinor superpositions can be represented by points on the Bloch sphere, which usually serves as a locus to depict all possible spin trajectories in the spin control or quantum computation. The spherical symmetry is preserved for isolated spins only. In semiconductors the main interaction mechanism between the spin and atomic orbitals comes from SO interaction, which may rearrange energy bands in the Brillouin zone and, depending on the wave vector symmetry group, simultaneously lift off Kramers pair splitting. As a result the spin trajectories cannot be represented on the Bloch sphere anymore. Nevertheless one can show that all possible spins (their directions and magnitudes) can still be mapped onto the closed spin surface in a three-dimensional spin space, the axes of which coincide with the real space Cartesian axes. This property allows one to describe spin dynamics in a self-evident manner in the real space rather than in an abstract Hilbert space.

To calculate spin surfaces of the individual subbands one must know spin matrices written in the same representation as the Hamiltonian (2). The method of construction of the required spin matrices was described in Ref. [33]. In the basis $|Jm_J\rangle = \left(|\frac{1}{2}\frac{1}{2}\rangle,|\frac{1}{2}\frac{\overline{1}}{2}\rangle,|\frac{3}{2}\frac{3}{2}\rangle,|\frac{3}{2}\frac{1}{2}\rangle,|\frac{3}{2}\frac{\overline{1}}{2}\rangle,|\frac{3}{2}\frac{\overline{3}}{2}\rangle,|\frac{1}{2}\frac{1}{2}\rangle,|\frac{1}{2}\frac{\overline{1}}{2}\rangle\right)$ one finds the following (8×8) Cartesian components of the spin vector matrix $\mathbf{S} = (S_x, S_y, S_z)$:

$$S_x = \left[\begin{array}{cc|cccc|cc} 0 & \frac{1}{2} & 0 & 0 & 0 & 0 & 0 & 0 \\ \frac{1}{2} & 0 & 0 & 0 & 0 & 0 & 0 & 0 \\ \hline 0 & 0 & 0 & \frac{1}{2\sqrt{3}} & 0 & 0 & \frac{1}{\sqrt{6}} & 0 \\ 0 & 0 & \frac{1}{2\sqrt{3}} & 0 & \frac{1}{3} & 0 & 0 & \frac{1}{3\sqrt{2}} \\ 0 & 0 & 0 & \frac{1}{3} & 0 & \frac{1}{2\sqrt{3}} & -\frac{1}{3\sqrt{2}} & 0 \\ 0 & 0 & 0 & 0 & \frac{1}{2\sqrt{3}} & 0 & 0 & -\frac{1}{\sqrt{6}} \\ \hline 0 & 0 & \frac{1}{\sqrt{6}} & 0 & -\frac{1}{3\sqrt{2}} & 0 & 0 & -\frac{1}{6} \\ 0 & 0 & 0 & \frac{1}{3\sqrt{2}} & 0 & -\frac{1}{\sqrt{6}} & -\frac{1}{6} & 0 \end{array}\right], \quad (18)$$

$$S_y = \left[\begin{array}{cc|cccc|cc} 0 & -\frac{\mathrm{i}}{2} & 0 & 0 & 0 & 0 & 0 & 0 \\ \frac{\mathrm{i}}{2} & 0 & 0 & 0 & 0 & 0 & 0 & 0 \\ \hline 0 & 0 & 0 & -\frac{\mathrm{i}}{2\sqrt{3}} & 0 & 0 & -\frac{\mathrm{i}}{\sqrt{6}} & 0 \\ 0 & 0 & \frac{\mathrm{i}}{2\sqrt{3}} & 0 & -\frac{\mathrm{i}}{3} & 0 & 0 & -\frac{\mathrm{i}}{3\sqrt{2}} \\ 0 & 0 & 0 & \frac{\mathrm{i}}{3} & 0 & -\frac{\mathrm{i}}{2\sqrt{3}} & -\frac{\mathrm{i}}{3\sqrt{2}} & 0 \\ 0 & 0 & 0 & 0 & \frac{\mathrm{i}}{2\sqrt{3}} & 0 & 0 & -\frac{\mathrm{i}}{\sqrt{6}} \\ \hline 0 & 0 & \frac{\mathrm{i}}{\sqrt{6}} & 0 & \frac{\mathrm{i}}{3\sqrt{2}} & 0 & 0 & \frac{\mathrm{i}}{6} \\ 0 & 0 & 0 & \frac{\mathrm{i}}{3\sqrt{2}} & 0 & \frac{\mathrm{i}}{\sqrt{6}} & -\frac{\mathrm{i}}{6} & 0 \end{array}\right], \quad (19)$$

$$S_z = \left[\begin{array}{cc|cccc|cc} \frac{1}{2} & 0 & 0 & 0 & 0 & 0 & 0 & 0 \\ 0 & -\frac{1}{2} & 0 & 0 & 0 & 0 & 0 & 0 \\ \hline 0 & 0 & \frac{1}{2} & 0 & 0 & 0 & 0 & 0 \\ 0 & 0 & 0 & \frac{1}{6} & 0 & 0 & -\frac{\sqrt{2}}{3} & 0 \\ 0 & 0 & 0 & 0 & -\frac{1}{6} & 0 & 0 & -\frac{\sqrt{2}}{3} \\ 0 & 0 & 0 & 0 & 0 & -\frac{1}{2} & 0 & 0 \\ \hline 0 & 0 & 0 & -\frac{\sqrt{2}}{3} & 0 & 0 & -\frac{1}{6} & 0 \\ 0 & 0 & 0 & 0 & -\frac{\sqrt{2}}{3} & 0 & 0 & \frac{1}{6} \end{array}\right]. \quad (20)$$

These matrices satisfy standard commutation relations, for example, $S_xS_y - S_yS_x = \mathrm{i}S_z$. The square of the vector $\mathbf{S}$ gives the diagonal matrix $\mathbf{S}^2 = (3/4)I$, where I is (8×8) unit matrix. Equations (18)–(20) show that conduction band edge multiplet, $J = 1/2$, is totally decoupled from the other bands.

Similarly one can introduce orbital surfaces that are related with the electron angular momentum operator $\mathbf{L}$. Introduction of such an object in solids is justified by the fact that normally the free electron or hole is propagating in one of the energy subbands that is doubly degenerate (Kramers pair), or split due to spin–orbit interaction, with spin-splitting energy $\Delta E(\mathbf{k})$ small as compared to the degeneracy energy $E(\mathbf{k})$. Thus, below for completeness we shall calculate the orbital surfaces. The respective components of the angular momentum matrix $\mathbf{L} = (L_x, L_y, L_z)$ can be calculated in a similar

manner as spin matrices. In the abovementioned basis they are

$$L_x = \left[\begin{array}{cc|cccc|cc} 0&0 & 0 & 0 & 0 & 0 & 0 & 0 \\ 0&0 & 0 & 0 & 0 & 0 & 0 & 0 \\ \hline 0&0 & 0 & \frac{1}{\sqrt{3}} & 0 & 0 & -\frac{1}{\sqrt{6}} & 0 \\ 0&0 & \frac{1}{\sqrt{3}} & 0 & \frac{2}{3} & 0 & 0 & -\frac{1}{3\sqrt{2}} \\ 0&0 & 0 & \frac{2}{3} & 0 & \frac{1}{\sqrt{3}} & \frac{1}{3\sqrt{2}} & 0 \\ 0&0 & 0 & 0 & \frac{1}{\sqrt{3}} & 0 & 0 & \frac{1}{\sqrt{6}} \\ \hline 0&0 & -\frac{1}{\sqrt{6}} & 0 & \frac{1}{3\sqrt{2}} & 0 & 0 & \frac{2}{3} \\ 0&0 & 0 & -\frac{1}{3\sqrt{2}} & 0 & \frac{1}{\sqrt{6}} & \frac{2}{3} & 0 \end{array}\right], \quad (21)$$

$$L_y = \left[\begin{array}{cc|cccc|cc} 0&0 & 0 & 0 & 0 & 0 & 0 & 0 \\ 0&0 & 0 & 0 & 0 & 0 & 0 & 0 \\ \hline 0&0 & 0 & -\frac{\mathrm{i}}{\sqrt{3}} & 0 & 0 & \frac{\mathrm{i}}{\sqrt{6}} & 0 \\ 0&0 & \frac{\mathrm{i}}{\sqrt{3}} & 0 & -\frac{2\mathrm{i}}{3} & 0 & 0 & \frac{\mathrm{i}}{3\sqrt{2}} \\ 0&0 & 0 & \frac{2\mathrm{i}}{3} & 0 & -\frac{\mathrm{i}}{\sqrt{3}} & \frac{\mathrm{i}}{3\sqrt{2}} & 0 \\ 0&0 & 0 & 0 & \frac{\mathrm{i}}{\sqrt{3}} & 0 & 0 & \frac{\mathrm{i}}{\sqrt{6}} \\ \hline 0&0 & -\frac{\mathrm{i}}{\sqrt{6}} & 0 & -\frac{\mathrm{i}}{3\sqrt{2}} & 0 & 0 & \frac{-2\mathrm{i}}{3} \\ 0&0 & 0 & -\frac{\mathrm{i}}{3\sqrt{2}} & 0 & -\frac{\mathrm{i}}{\sqrt{6}} & \frac{2\mathrm{i}}{3} & 0 \end{array}\right], \quad (22)$$

$$L_z = \left[\begin{array}{cc|cccc|cc} 0&0 & 0 & 0 & 0 & 0 & 0 & 0 \\ 0&0 & 0 & 0 & 0 & 0 & 0 & 0 \\ \hline 0&0 & 1 & 0 & 0 & 0 & 0 & 0 \\ 0&0 & 0 & \frac{1}{3} & 0 & 0 & \frac{\sqrt{2}}{3} & 0 \\ 0&0 & 0 & 0 & -\frac{1}{3} & 0 & 0 & \frac{\sqrt{2}}{3} \\ 0&0 & 0 & 0 & 0 & -1 & 0 & 0 \\ \hline 0&0 & 0 & \frac{\sqrt{2}}{3} & 0 & 0 & \frac{2}{3} & 0 \\ 0&0 & 0 & 0 & \frac{\sqrt{2}}{3} & 0 & 0 & -\frac{2}{3} \end{array}\right]. \quad (23)$$

As it should be, these matrices also satisfy standard commutation relations $L_xL_y - L_yL_x = \mathrm{i}L_z$, etc. The zeros in the upper (4×4) diagonal blocks are in agreement with the fact that the conduction band is made of s-type atomic orbitals. The total angular momentum, $\mathbf{J} = \mathbf{L}+\mathbf{S}$, is equal to the sum of the above constructed L_i and S_i matrices. Since the Hamiltonian (17) is in the total angular momentum $\mathbf{J}$ representation, the matrix $J_z = L_z + S_z$, as can be checked by adding matrices (23) and (20), is diagonal with elements on the diagonals that represent $J = 1/2$, $3/2$, and $1/2$ multiplets that correspond to conduction, valence, and spin–orbit split-off bands.

4. Parametrization of 2D wave functions

In interpreting various physical properties of semiconductors it is a common practice to use energy representation, where band properties are described by dispersion law $E_i(\mathbf{k})$, with i being the band index. To find all possible spin superpositions states in the ith band at wave vector $\mathbf{k}$ we shall use the energy representation and will parametrize the considered ith Kramers pair (energy band) in the following way:

$$|\varphi(\Gamma_i)\rangle = \cos\vartheta|\varphi(\Gamma_i^{-m_J})\rangle + \sin\vartheta\,\mathrm{e}^{\mathrm{i}\phi}|\varphi(\Gamma_i^{m_J})\rangle\,, \quad (24)$$

where $m_J = 1/2$ or $3/2$, and the parameters ϑ and ϕ define the amplitude and phase in the superposition of spin states. As mentioned, it will be assumed that only one doubly degenerate or nearly degenerate Kramers pair is occupied by free charge carrier. The required band dispersion laws $E_i(\mathbf{k})$, where i indicates $\Gamma_8^{\pm1/2}$, $\Gamma_8^{\pm3/2}$, $\Gamma_7^{\pm1/2}$, or $\Gamma_6^{\pm1/2}$ band, can be found by diagonalizing the Hamiltonian (2) with an appropriate (8×8) unitary matrix U:

$$U^\dagger H U \equiv H_E = \mathrm{diag}\left[2E_{\Gamma_8^{\pm1/2}}, 2E_{\Gamma_8^{\pm1/2}}, 2E_{\Gamma_6^{\pm1/2}}, 2E_{\Gamma_7^{\pm1/2}}\right], \quad (25)$$

where "diag" indicates the diagonal (8×8) matrix, with pairs of bands having the same point group symmetry. In the energy representation (25), in the order of decreasing eigenenergies, the parametrized spinors have the following forms:

$$|\varphi(\Gamma_8^{\pm1/2})\rangle = (\cos\vartheta, \sin\vartheta\,\mathrm{e}^{\mathrm{i}\phi}, 0, 0, 0, 0, 0, 0)\,, \quad (26a)$$

$$|\varphi(\Gamma_8^{\pm3/2})\rangle = (0, 0, \cos\vartheta, \sin\vartheta\,\mathrm{e}^{\mathrm{i}\phi}, 0, 0, 0, 0)\,, \quad (26b)$$

$$|\varphi(\Gamma_6^{\pm1/2})\rangle = (0, 0, 0, 0, \cos\vartheta, \sin\vartheta\,\mathrm{e}^{\mathrm{i}\phi}, 0, 0)\,, \quad (26c)$$

$$|\varphi(\Gamma_7^{\pm1/2})\rangle = (0, 0, 0, 0, 0, 0, \cos\vartheta, \sin\vartheta\,\mathrm{e}^{\mathrm{i}\phi})\,. \quad (26d)$$

The parameters ϑ and ϕ have no influence on the band eigenenergies. By selecting the concrete values of ϑ and ϕ one fixes different mixing ratios and phase relations between the Kramers doublets. With the help of the parameters ϑ and ϕ one can change the magnitude and spin direction of carrier that propagates in a particular subband with a given wave vector $\mathbf{k}$. The required unitary matrix U can be constructed from the eigenfunctions of the considered Hamiltonian (17) [34]. If U is known, the spinor in the initial J_z representation (1) then will be

$$|\psi(\vartheta,\phi)\rangle = U|\varphi(\vartheta,\phi)\rangle\,. \quad (27)$$

In the following we shall be interested in the quantum mechanical average spin $\langle\mathbf{S}\rangle$. Mathematically the

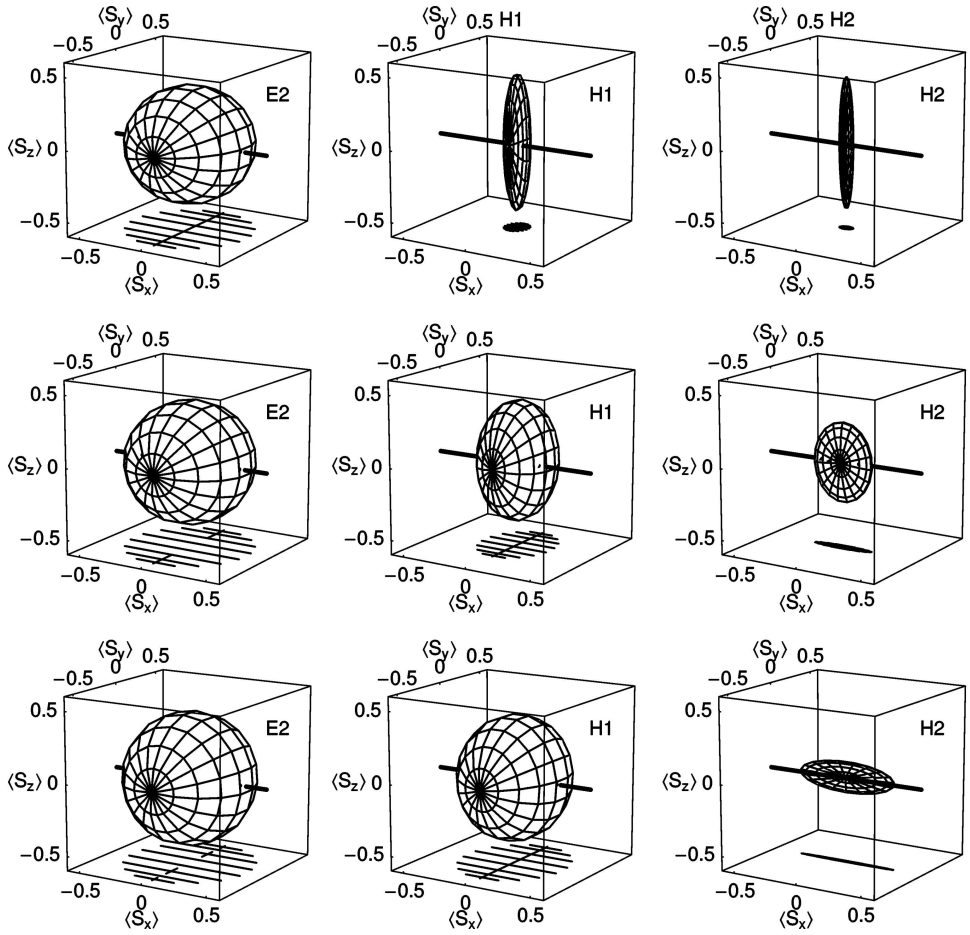

Fig. 6. Spin surfaces and their horizontal projections for E2, H1, and H2 subbands (columns). The QW lies in x–y plane. The direction of the wave vector $\mathbf{k}$ is shown by lines, $\mathbf{k}||[10]$. Its magnitude for, respectively, upper, middle, and bottom rows is $|\mathbf{k}| = 0.06$, 0.15, and $0.3\ \mathrm{nm}^{-1}$.

spin surface represents all possible realizations of $\langle \mathbf{S} \rangle$, when the parameters ϑ and ϕ are allowed to vary,

$$\langle \mathbf{S}(\vartheta, \phi) \rangle = \langle \psi(\vartheta, \phi) | \mathbf{S} | \psi(\vartheta, \phi) \rangle, \qquad (28)$$

where $\mathbf{S}$ is given by matrices (18)–(20). As mentioned, the spinor $|\psi\rangle$ represents all possible superpositions of "up" and "down" spin eigenstates in the Kramers pair. The same parametrized spinors (26) were used to find orbital surfaces $\langle \mathbf{L}(\vartheta, \phi) \rangle$.

5. Spin and orbital surfaces

Figures 6 and 7 show spin surfaces $\langle \mathbf{S}(\vartheta, \varphi) \rangle$ for three energy subbands when $\mathbf{k}||[10]$ and $\mathbf{k}||[11]$ and their transformation when the in-plane wave vector $\mathbf{k}$ increases. To draw the spin surface at a selected $\mathbf{k}$, at first the eigenvectors were calculated numerically from the total 2D Hamiltonian and the unitary matrix U was constructed. The application of U to the parametrized superposition of type (26) gave the spinors in J_z representation having two parameters ϑ and ϕ. In the figures, the parallels and meridians that visualize spin surfaces correspond to either $\vartheta = \mathrm{const}$ or $\phi = \mathrm{const}$, respectively. The straight line (not shown in the figures) that connects two singular points (poles) on the spin surface represents the natural quantization axes of the problem. It is seen that in the considered case the quantization axes lie in the QW plane and are perpendicular to $\mathbf{k}$. If the spin-splitting is neglected ($H_{\mathrm{R}} = 0$) the subbands become degenerate and, as a result, the quantization axis is not fixed in the spin space. In the numerical calculations its direction, in fact, is determined by algorithm used. In the present calculations the quantization axis (not the orientation of the spin surface in the spin space) has aligned automatically with $\langle S_z \rangle$ when H_{R} has been switched off. It should be stressed once more that the spin surface is a universal characteristic: neither its shape nor alignment in the spin space does depend on the concrete values of the spin-splitting energy ΔE as long as $\Delta E \ll E$. Thus, on the dispersion curve in the vicinity of the degeneracy point E the spin surface will represent all allowed directions

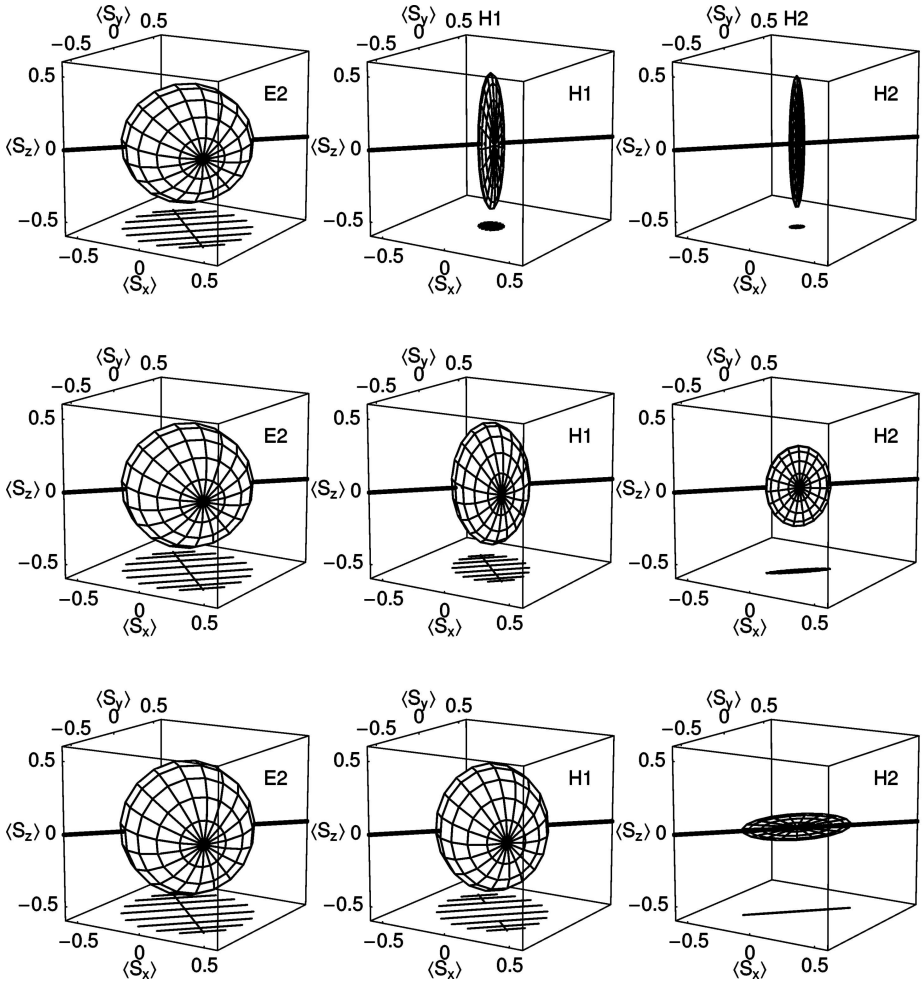

Fig. 7. The same as in Fig. 6 but for $\mathbf{k}\|[11]$.

and magnitudes of the injected spins into the spin FET channel. In the experiment, the concrete direction and magnitude of $\langle \mathbf{S} \rangle$ will be selected by spin injector.

The first columns in the Figs. 6 and 7 show that, independent of electron energy, the shape of the spin surface in E2 subband does not depend on $\mathbf{k}$ and is very close to the Bloch sphere. Therefore, E2 electron spin dynamics to high accuracy can be described by the standard precession equation

$$\frac{\mathrm{d}\langle \mathbf{S} \rangle}{\mathrm{d}t} = -\mathbf{\Omega} \times \langle \mathbf{S} \rangle \,, \tag{29}$$

where $\mathbf{\Omega}$ is the precession vector parallel to the natural quantization axis. The modulus of $\mathbf{\Omega}$ is equal to the spin-splitting energy ΔE divided by Planck's constant $\hbar$. The spherical symmetry of E2 subband is related with the fact that it originates from s-like atomic orbitals of the bulk conduction band (the band $\Gamma_6^{\pm 1/2}$ in Fig. 1(b)). In Ref. [19] it has been shown that the sphericity of the electron spin surfaces in A_3B_5 QW's is satisfied to high accuracy: the difference in lengths of the fundamental spin surface ellipsoidal axis appear to be smaller than 0.1%. From this it may be concluded that the free electron spin dynamics (for example, the precession represented by circles around the quantization axis, or spin echoes of the ensemble of spins) in E2 subband will be exactly the same as in the standard EPR or NMR experiments, where, as known, the dynamics of an ensemble of spins could be completely described by average spin trajectories on the Bloch sphere.

In Figs. 6 and 7 the second columns show that in the electronic H1 subband there is a large admixture of p-type atomic orbitals, since the spin surface shape strongly depends on the charge carrier wave vector. This property has been found earlier for heavy-mass holes in bulk A_3B_5 semiconductors, in which the valence band consists entirely of p-atomic orbitals [18, 35]. At small wave vectors the spin surface is needle-like and reduces to a line at $\mathbf{k} = 0$, however it blows up to the Bloch sphere when the free carrier energy becomes large enough. This indicates that H1 indeed

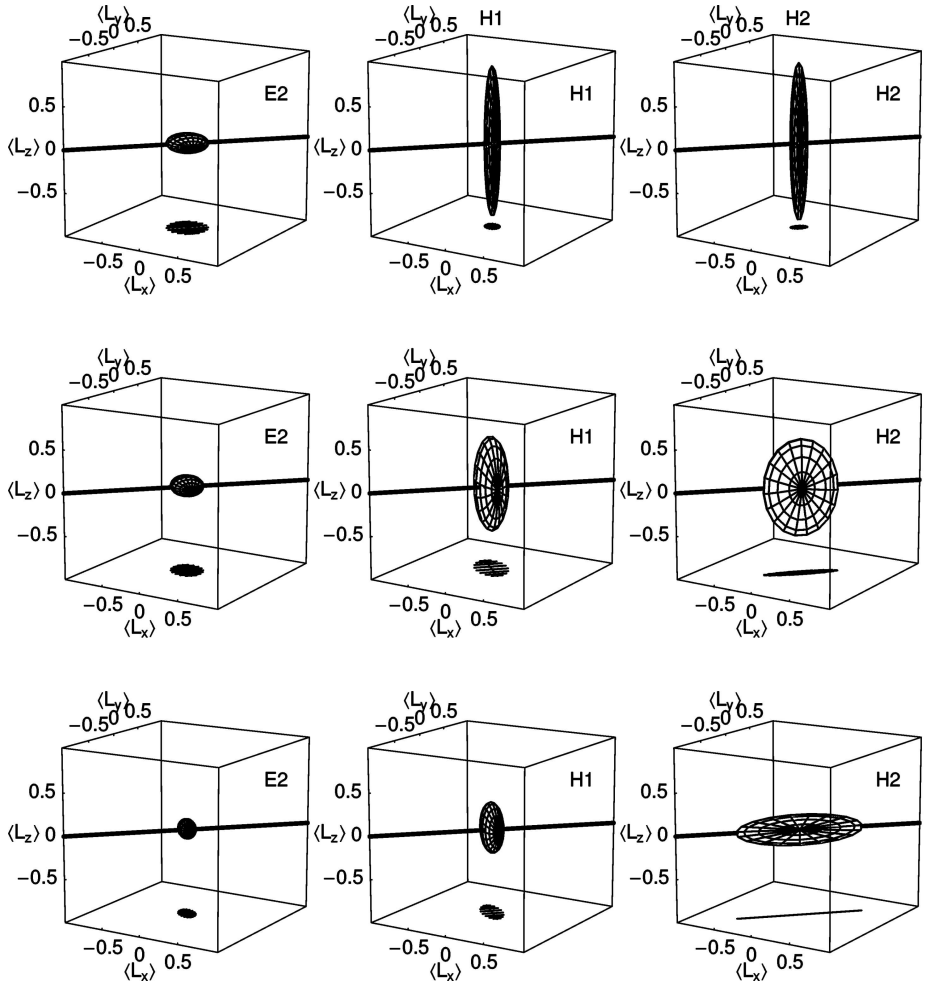

Fig. 8. Orbital surfaces and their horizontal projections for E2, H1, and H2 subbands (columns). The QW lies in x–y plane. The direction of wave vector $\mathbf{k}\|[11]$ is shown by lines. The magnitude of $\mathbf{k}$ is, respectively, for the upper, middle, and bottom rows: $|\mathbf{k}| = 0.06$, 0.15, and 0.3 nm^{-1}.

originates from the bulk valence band spinors at small energies and from the conduction band spinors at large energies. If the electron injected into H1 subband appears to have small energy, its spin polarization will always be linear and parallel to QW normal. From this follows that to have an efficient spin injection into this subband the injector should have vertical rather than horizontal polarization. Furthermore, the average spin precession trajectories of such injected electrons cannot be described by the standard precession Eq. (29). Now the trajectories, as it is suggested by the spin surface of H1 subband, will assume the shape of elongated ellipses. In the case of A_3B_5 holes, the respective precession equations (analogues of Eq. (29)) were given in Refs. [18, 35] for various directions of $\mathbf{k}$. Strong deviation of spin surface shape from spherical one explains why in the experiments it is difficult to observe free electron EPR under thermal carrier distribution.

In the H2 subband (the fundamental hole subband), as the third columns in Figs. 6 and 7 demonstrate, the spin surfaces are needle-shaped at low hole energies and disc-shaped at high energies. In the latter case all possible spin polarizations will stretch out on a flat surface. However, the surface does not possess rotational symmetry with respect to the wave vector. The Figs. 6 and 7 also suggest that the spin surface rotates synchronously with the in-plane wave vector $\mathbf{k}$. A more detailed comparison between the spin surface projections on $\langle S_x\rangle$–$\langle S_y\rangle$ plane as well as on other symmetry planes allows one to conclude that possible variance in the spin surface shape is very small, if any, for different $\mathbf{k}$ directions when $|\mathbf{k}| = \mathrm{const}$. Thus, the shape of the spin surface is mainly determined by the magnitude of $\mathbf{k}$ and selected energy subband.

Figure 8 shows the orbital surfaces calculated under similar conditions. For an s-type atomic orbital, as it is well known, one has $\mathbf{L} = 0$, and as a result the orbital surface should shrink to a point. As can be seen from

the first column, however, due to very small admixture of p-atomic orbitals, the surface has a finite volume albeit of small magnitude. From this it may be concluded that orbital rather than spin surface is more sensitive to small admixture of p-type orbitals. The second and third columns show that orbital surface shapes of other subbands strongly depend on $|\mathbf{k}|$.

Since the total angular momentum is $\mathbf{J} = \mathbf{L} + \mathbf{S}$, the Figs. 7 and 8 can be used to build the corresponding surfaces for the total angular momentum $\langle \mathbf{J} \rangle = \langle \mathbf{L} \rangle + \langle \mathbf{S} \rangle$. The latter visualizes all allowed values and directions of the average $\mathbf{J}$.

6. Conclusions

In the inverted HgTe QWs the spin surfaces may have various shapes – spherical, ellipsoidal, disk-, or even needle-like. The shape of the spin surface depends on QW composition [36] and free carrier wave vector but is independent of a particular SO interaction mechanism used (Rashba or QW asymmetry in electric field). In 2D conduction subbands, the spherical shape is preserved only for high energy electrons. The spin surface of the fundamental conduction subband transforms from linear to spherical shape when electron energy increases. This property comes from band inversion and is absent in normal gap A_3B_5 and A_2B_6 QWs, where the energy gap is positive. The spin surfaces of 2D valence subbands, in general, were found to be nonspherical. The nonsphericity is related with the transformation of the valence band in the centre of the Brillouin zone and the dependence on the charge carrier wave vector.

The knowledge of the spin surface shape allows one to envisage spin precession trajectories of ballistic carriers. This is important in designing spintronics devices and in understanding global spin properties of charge carriers injected into spin-FET channel or spin waveguide as well as in predicting spin matching conditions, for example, between the spin injector and channel. Of particular interest may be the needle-like spin surfaces at low carrier energies. The charge carriers with such surfaces allow one to achieve linear rather than circular time-dependent spin polarization.

Acknowledgement

The work was partly supported by the Lithuanian State Science and Studies Foundation under contract C-07004.

References

[1] I. Žutić, J. Fabian, and S. Das Sarma, Spintronics: Fundamentals and applications, Rev. Mod. Phys. **76**(2), 323–410 (2004).

[2] R.H. Silsbee, Spin-orbit induced coupling of charge current and spin polarization, J. Phys. Cond. Matter **16**(7), R179–R207 (2004).

[3] T. Jungwirth, J. Sinova, J. Mašek, J. Kučera, and A.H. MacDonald, Theory of ferromagnetic (III,Mn)V semiconductors, Rev. Mod. Phys **78**(3), 809–864 (2006).

[4] A. Dargys, Why the spin-FET does not work?, Lithuanian J. Phys. **47**(2), 185–194 (2007).

[5] L. Allen and J.H. Eberly, *Optical Resonance and Two-Level Atoms*, (Wiley–Interscience, New York, 1975), ch. 2.

[6] S. Datta and B. Das, Electronic analog of the electro-optic modulator, Appl. Phys. Lett. **56**(2), 665–667 (1990).

[7] I. Appelbaum and D.J. Monsma, Transit-time spin field-effect transistor, Appl. Phys. Lett. **90**(26), 262501-1–3 (2007).

[8] B. Huang, D.J. Monsma, and I. Appelbaum, Experimental realization of a silicon spin field-effect transistor, Appl. Phys. Lett. **91**(7), 072501-1–3 (2007).

[9] B.A. Bernevig, T.L. Hughes, and S.C. Zhang, Quantum spin Hall effect and topological phase transition in HgTe quantum wells, Science **314**(Dec.), 1757–1761 (2006).

[10] M. König, S. Wiedmann, C. Brühne, A. Roth, H. Buhmann, L.W. Molenkamp, X.-K. Qi, and S.C. Zhang, Quantum spin Hall insulator state in HgTe quantum wells, Science **318**(Nov.), 766–770 (2007).

[11] M.H. Weiler, in: *Semiconductors and Semimetals*, eds. R.K. Willardson and A.C. Beer, Vol. 16 (Academic Press, New York, 1981), pp. 119–191.

[12] M. Schultz, F. Heinrichs, U. Merkt, T. Colin, T. Skauli, and S. Løvold, Rashba spin splitting in a gated HgTe quantum well, Semicond. Sci. Technol. **11**(8), 1168–1172 (1996).

[13] K. Ortner, X.C. Zhang, A. Pfeuffer-Jeschke, C.R. Becker, G. Landwehr, and L.W. Molenkamp, Valence band structure of HgTe / $Hg_{1-x}Cd_xTe$ single quantum wells, Phys. Rev. B **66**(7), 075322-1–6 (2002).

[14] V.F. Radantsev and A.M. Yafyasov, Rashba splitting in HgCdTe MIS-structures, Zh. Eksp. Teor. Fiz. **122**(3), 570–581 (2002) [in Russian]; English translation: JETP **95**(3), 491–501 (2002).

[15] C.R. Becker, X.C. Zhang, A. Pfeuffer-Jeschke, K. Ortner, V. Hock, G. Landwehr, and L.W. Molenkamp, Very large Rashba spin-orbit splitting in HgTe quantum wells, J. Supercond. Incorp. Novel Magn. **16**(4), 625–634 (2003).

[16] Y.S. Gui, C.R. Becker, N. Dai, J. Liu, Z.J. Qiu, E.G. Novik, M. Schäfer, X.Z. Shu, J.H. Chu,

H. Buhmann, and L.W. Molenkamp, Giant spin-orbit splitting in a HgTe quantum well, Phys. Rev. B **70**(11), 115328-1–5 (2004).

[17] J. Hinz, H. Buhmann, M. Schäfer, V. Hock, C.R. Becker, and L.W. Molenkamp, Gate control of the giant Rashba effect in HgTe quantum wells, Semicond. Sci. Technol. **21**(4), 501–506 (2006).

[18] A. Dargys, Precession trajectories of the hole spin in zinc-blende semiconductors, Solid-State Electron. **51**(1), 93–100 (2007).

[19] A. Dargys, Free-electron spin surfaces in 3D and 2D zinc-blende semiconductors, Phys. Status Solidi B **243**(8), R54–R56 (2006).

[20] A. Dargys, Spin properties of 2D charge carriers in semiconductors with inverted bands, Europhys. Lett. **81**(3), 38003-1–4 (2008).

[21] M.G. Burt, The justification for applying the effective-mass approximation to microstructures, J. Phys. Cond. Matter **4**(32), 6651–6690 (1992).

[22] B.A. Foreman, Effective-mass Hamiltonian and boundary conditions for the valence bands of semiconductor microstructures, Phys. Rev. B **48**(7), 4964–4967 (1993).

[23] E.G. Novik, A. Pfeuffer-Jeschke, T. Jungwirth, V. Latussek, C.R. Becker, G. Landwehr, H. Buhmann, and L.W. Molenkamp, Band structure of semimagnetic $Hg_{1-y}Mn_yTe$ quantum wells, Phys. Rev. B **72**(3), 035321-1–12 (2005).

[24] J.P. Laurenti, J. Camassel, and A. Bouhemadou, Temperature dependence of the fundamental absorption edge of mercury cadmium telluride, J. Appl. Phys. **67**(10), 6454–6460 (1990).

[25] R. Wollrab, R. Sizmann, F. Koch, J. Ziegler, and H. Maier, Spin splitting of the electron subbands in the electrostatic interface potential on HgCdTe, Semicond. Sci. Technol. **4**(6), 491–494 (1989).

[26] X.C. Zhang, K. Ortner, A. Pfeuffer-Jeschke, C.R. Becker, and G. Landwehr, Effective g factor of n-type $HgTe/Hg_{1-x}Cd_xTe$ single quantum wells, Phys. Rev. B **69**(11), 115340-1–7 (2004).

[27] X.C. Zhang, A. Pfeuffer-Jeschke, K. Ortner, V. Hock, H. Buhmann, C.R. Becker, and G. Landwehr, Rashba splitting in n-type modulation-doped HgTe quantum wells with an inverted band structure, Phys. Rev. B **63**(24), 245305-1–8 (2001).

[28] R. Winkler, *Spin-Orbit Coupling Effects in Two-Dimensional Electron and Hole Systems* (Springer-Verlag, Berlin–Heidelberg, 2003).

[29] G. Dresselhaus, Spin-orbit coupling effects in zinc blende structures, Phys. Rev. **100**(2), 580–586 (1955).

[30] F. Boxberg and J. Tulkki, Theory of the electronic structure and carrier dynamics of strain-induced (Ga,In)As quantum dots, Rep. Prog. Phys. **70**, 1425–1471 (2007).

[31] G.H. Golub and C.F. Van Loan, *Matrix Computations* (The John Hopkins University Press, Baltimore and London, 1989).

[32] C. Kittel, *Quantum Theory of Solids* (John Wiley & Sons, New York, 1963), ch. 9.

[33] M. Abolfath, T. Jungwirth, J. Brum, and A.H. MacDonald, Theory of magnetic anisotropy in $III_{1-x}Mn_xV$ ferromagnets, Phys. Rev. B **63**(5), 054418-1–14 (2001).

[34] M. Tinkham, *Group Theory and Quantum Mechanics* (McGraw–Hill, Inc, New York, 1964), appendix.

[35] A. Dargys, Free-hole spin precession trajectories in A_3B_5 compounds, in: *Advanced Optical Materials, Technologies, and Devices*, eds. S. Ašmontas and J. Gradauskas, Proc. SPIE **6596**, 65960O-1–6 (2007).

[36] A. Dargys, Spin properties of $Hg_{1-x}Cd_xTe/CdTe$ quantum wells, Phys. Status Solidi B (2008) [accepted].

KVANTINIO $Hg_{1-x}Cd_xTe/CdTe$ ŠULINIO LAISVŲJŲ ELEKTRONŲ BEI SKYLIŲ SUKINIO SAVYBĖS

A. Dargys

Puslaidininkių fizikos institutas, Vilnius, Lietuva

Santrauka

Pasitelkus aštuonių juostų $\mathbf{k}\cdot\mathbf{p}$ hamiltonianą, išnagrinėtos $Hg_{1-x}Cd_xTe/CdTe$ kvantinių šulinių su invertuotomis energijos juostomis sukinio savybės. Energijos juostų suskilimas, susijęs su sukinio laisvės laipsniu ir Kramerso poromis, buvo įskaitytas arba per Rashbos hamiltonianą, arba per išorinio lauko hamiltonianą. Išnagrinėti sukinio paviršių, kurie nusako sukinio dydžio priklausomybę nuo jo krypties, pavidalai. Parodyta, kad balistinių dvimačių elektronų sukinio paviršiai bendru atveju turį elipsoidinį, o ne labiau įprastą sferinį pavidalą. Ribiniais atvejais sukinio paviršiai gali transformuotis į diską, tiesę arba Blocho sferą. Grafiškai pateiktos dvimačių elektronų ir skylių sukinio paviršių formos sukinio erdvėje, esant įvairiems laisvojo krūvininko bangos vektoriams ir skirtingoms kvantinį šulinį sudarančio junginio $Hg_{1-x}Cd_xTe$ sudėtims.